Available online at www.sciencedirect.com
SCIENCE DIRECT®
Polymer 45 (2004) 2603–2613
polymer
www.elsevier.com/locate/polymer

# Morphological distribution of injection-moulded isotactic polypropylene: a study of synchrotron small angle X-ray scattering

Peng-wei Zhu*, Graham Edward

*School of Physics and Materials Engineering, CRC for Polymers, Monash University, Wellington, Clayton, Vic. 3800, Australia*

Received 25 November 2003; received in revised form 5 February 2004; accepted 18 February 2004

**Abstract**

Synchrotron small-angle X-ray scattering (SAXS) studies were carried out to investigate effects of thickness of injection-moulded isotactic polypropylene (iPP) plates on shear-induced morphology and morphological distribution through the depth direction of the plates. Different levels of effective shear flow are imposed on the iPP melt by changing the thickness of the plates although the injection moulding is performed with the same injection ram speed and the same melt and mould temperatures. Shish-kebab-like morphology is found roughly 100 μm from the surface of plates, regardless of the thickness of plates. However, the type of shish-kebab-like morphology is very sensitive to the thickness. The shish-kebab structure at the surface region can be changed into the kebab-structure only or random crystalline lamellae as the thickness of the plate increases. The preferential orientation of crystalline lamellae along the flow direction strongly depends on the thickness of the plate, although the melt-shear does not significantly enhance the degree of linear crystallinity. It is also found that in the core region, the slow relaxation of polymer chains in the thick plate results in a higher degree of linear crystallinity. The results indicate that the shear-induced morphology is strongly dependent on effective shear flow and should be described individually.


*Keywords:* Morphological distribution; Shear flow; Synchrotron radiation

## 1. Introduction

Semicrystalline polymers are technologically important as they comprise about two-thirds of the global polymer production and have wide ranging applications [1]. Processing of semicrystalline polymers involves the imposition of varying levels of flow fields (shear, elongation, and mixed) on molten polymers at different stages of the processing [1]. These flow fields can introduce different degrees of anisotropy to polymer melts, which significantly accelerates the nucleation rate of the crystallization process. As a result, the effects of flow fields on polymer melts alter morphology, morphological distribution, and product properties as well. In most polymer processing operations, such as injection moulding, extrusion, and fiber spinning, the morphology and its distribution of resultant polymer products are deeply influenced by molecular orientation induced by the flow (in the molten state) and the deformation (in the solid state). It is found, for example, that flow-induced crystallization of polymer melts results in the formation of shish-kebab morphology that has attracted attention since the 1970s [2–5]. A number of different models have been proposed to describe the structures during or subsequent to the imposition of melt flow [6–8]. The shear-induced crystallization of polymer melts can be found due to a broad range of shearing rates from a laboratory scale to industrial processing. The shear flow of industrial processing is often considered as relatively weak and that it may not easily induce the formation of very extended polymer chains. However, there is no doubt that the shear flow of industrial processing operations can modify the crystallization and the resulting morphology of semicrystalline polymers [9–16].

The morphology of injection-moulded isotactic poly(propylene) (iPP) is found to be a skin-core structure in which multiple layers have been observed by light microscopy [9–16]. The hot iPP melt contacting with the cold walls of the die experiences high stresses, strain rates and cooling rates and subsequently the final structures are inhomogeneous and anisotropic. The layer numbers and thickness of injection-moulded iPP may vary from one semicrystalline polymer to another and the structures are

* Corresponding author. Tel.: +61-399-059-981; fax: +61-399-054-940.
*E-mail address:* peng.zhu@spme.monash.edu.au (P. Zhu).

0032-3861/$ - see front matter © 2004 Elsevier Ltd. All rights reserved.
doi:10.1016/j.polymer.2004.02.031

pronouncedly dependent on moulding conditions. Nevertheless, at least three different regions have been observed when thin sections of mouldings are examined using optical microscopy. The skin region is often considered to be very thin and essentially characterized by a relatively high amorphous content due to rapid cooling. The lower cooling rate in the core region can allow complete relaxation of the chain molecules and the growth of spherulites. The skin and core regions are generally separated by a shear zone or surface region.

Among the variety of oriented arrangement of morphologies that may occur during shear-induced crystallization of polymer melts, the shish-kebab structure has attracted special attention. The description of morphology of injection-moulded iPP in terms of the shish-kebab model has been proposed [17–20]. The lamellar kebabs are held together by the tie molecules of the shish, and both the crystallites and the tie molecules have preferred *c*-axis orientation along the flow direction. Taken on its own, the original shish-kebab model alone may not well explain the bimodal orientation often found in injection-moulded iPP. It has been suggested that the lamellar structure near the surface can be characterized by a 'parent–daughter' or a bimodal orientation model [21–24]. In terms of the parent–daughter model, the parent and daughter lamellae can be linked by tie molecules along the flow direction, but the parent and daughter lamellae have quite different but related *c*-axis orientations. The parent lamellae have folding chains with their *c*-axis preferentially aligned along the flow direction while the daughter lamellae have their *a**-axis (originated by *a*-axis of the daughter lamellae) parallel to the parent *c*-axis, having epitaxially grown from the parent. Compared with the parent lamellae, the daughter lamellae are small and imperfect, and the size of daughter lamellae is not uniform. The *b*-axis of the daughter lamellae is parallel to the *b*-axis of the parent lamellae, and the tilt angle between the parent and daughter lamellae is found to be 80° [25,26].

The final morphology and its distribution of injection-moulded iPP articles are pronouncedly dependent on moulding conditions, including processing temperature, injection speed and pressure, holding pressure, and cooling time [27]. A fine balance between flow shear and other moulding conditions can lead to improved properties of designed materials. The molecular nature of iPP, such as molecular weight and its distribution, chain branching, and the presence of nucleating agents also play important roles [28–30]. It is worth noting that most experiments reported here were not carried out under industrial processing conditions in which the shear flow is relatively weak. The purpose of this paper is to explore the effects of the thickness of injection-moulded iPP plate on the morphological distribution, including lamellar orientation and dimensions, through the thickness of the plate. The external shear is controlled to be the same under the injection moulding conditions, whereas the levels of effective melt-shear internally imposed on the polymer melt are changed when the melt flows through dies with different thickness. The morphologies and morphological distributions, which are frozen in the solid state, would subsequently develop in different ways with the depth of plate. Highly collimated synchrotron small angle X-ray scattering (SAXS) was used to characterize accurately the morphological development through the plate depth with high spatial resolution at a selected position of iPP plates. Since the shear-induced crystallization of injection-moulded plates starts from the surface region and propagates toward the core region, the morphological distribution through the depth of the plate can provide tracks of the shear effect on the crystallization.

## 2. Experimental

A commercial iPP (Basell Moplen EP301K) was used to mould end-gated plates, as shown in Fig. 1. According to the manufacturer, the raw material has the standard process stability suitable for injection moulding. The melt flow rate of the raw material is 4. Rectangular plates of iPP with a length *l* of 130 mm, width *w* of 73 mm, and thickness *h* (1, 3, and 5 mm) were injection moulded with conditions as follows: melt temperature 215 °C, mold temperature 47 °C, holding pressure 40 MPa, holding time 12 s, and cooling time 20 s. The maximum shear strain rate (at the wall) of a non-Newtonian flow through a rectangular channel can be given as follows [31]:

$$\dot{\gamma}_{\text{wall}} = \frac{(2n+1)}{n}\frac{2Q}{wh^2} \tag{1}$$

where $Q$ is the flow rate and $n$ a flow behavior index. If it is assumed that the flow rate $Q$ is a constant, the ratios of the

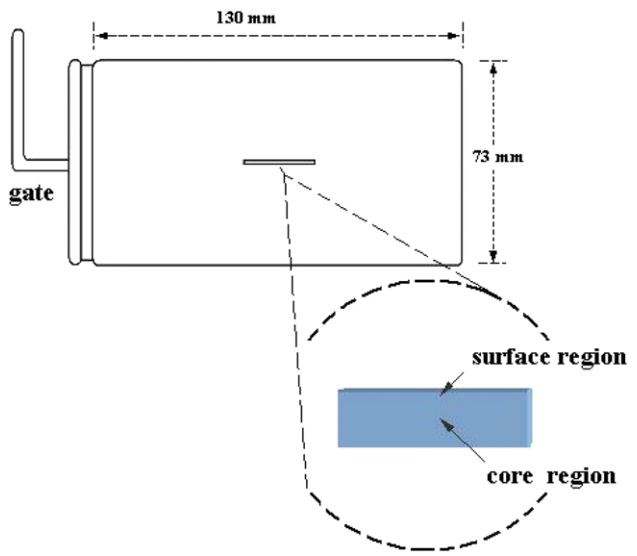


Fig. 1. A schematic diagram of an injection-moulded plate and the injection moulded iPP specimen cut at a central position away from the gate. The plane of the specimens is parallel to the flow direction and the X-ray beam is then normal to flow direction.

maximum shear strain rate are 1:0.58:0.45, corresponding to plate thicknesses $h = 1$, 3, and 5 mm, respectively. The maximum shear strain rate decreases significantly with an increase in the thickness of the plate, which would alter the morphology and morphological distribution.

The injection moulded iPP specimens were cut at a central position away from the gate, as indicated in Fig. 1, with a length of 10 mm, depth of 1.0 mm, and three widths of 1, 3, and 5 mm. These specimens were respectively named as iPP-1, iPP-3, and iPP-5, corresponding to plate thickness of 1, 3, and 5 mm, respectively. The plane of the specimens used is parallel to the flow direction.

The X-ray scattering experiments were performed at room temperature at the Australian National Beamline Facility (ANBF), a synchrotron beam-line at the Photon Factory in Tsukuba, Japan. The ANBF is installed on a bending magnet port, and delivers monochromatic synchrotron X-rays in the energy range 4.5–20 keV to the experimental station in a hutch. The instrument has a multi-configuration vacuum diffractometer that uses image plates as its detector system. The square-shaped micro-beam had a dimension of $200 \times 200\ (\mu m)^2$. The wavelength of 2.0 Å was employed to record 2D SAXS image patterns.

The iPP specimens were mounted at the centre of ANBF vacuum diffractometer with the specimens 570 mm from the image plate. Measurements were performed with the primary beam being perpendicular to the flow direction and the scattering being measured along a direction normal to the layered planes in the moulding. The beam passed through the specimen and the illuminated zone was changed with a vertical shift of the sample holder along the direction of plate thickness (or specimen width). Only one half width of each specimen was illuminated. Physical parameters calculated later will be plotted as a function of the depth through the plate thickness on the assumption that the morphology at the same distance from surfaces of the plate is the same or the distribution is symmetrical. The steps of vertical shift of the illuminated zone were chosen so that more X-ray patterns were obtained from the surface region. For all specimens, the first measurement was always taken with the beam centre 100 μm from the surface. The scattering at 100 μm is low simply because the illuminated area is small. This step should not be taken as a measurement of the skin as the X-ray beam cannot access the specimen skin in the present experiments.

The integrated intensity of 2D image patterns was obtained using PPDA software. The 'box sizes' of PPDA (or the integrated areas) are set to be 45 and 230 for the integration of equatorial and meridional scattering, respectively. The horizontal 'box' is for the integration of equatorial scattering and vertical for the integration of meridional scattering. The dimensions of 'box size' were consistently applied for all the positions of every sample. The scattered intensity was then presented as a function of scattering vector $q$ where $q = 4\pi\sin(\theta)/\lambda$. Scattering without the specimen was recorded as a background scattering $I_b$, to enable correction of measured SAXS patterns.

## 3. Results and discussion

Fig. 2(a) shows a selected 2D SAXS image pattern (the flow direction is vertical) recorded at a depth of 100 μm in an iPP-3 moulding. This image represents the raw pattern without background correction. The very strong scattering, which is also observed from background pattern (Fig. 2(b)), is due to guard slits. Two distinct scattering maxima along and normal to the flow direction can be seen, which indicate morphological orientation at this depth of iPP-3. Fig. 2(a) is sectioned into two parts, as shown in Fig. 2(c), for the calculation of oriented SAXS intensities, namely meridional scattering $I_{meridian}$ and equatorial scattering $I_{equator}$, after subtraction of background scattering from the pattern. The meridional maxima in the SAXS pattern can be attributed to the formation of kebab-like lamellar structures that are spatially uncorrelated and perpendicular to the flow direction whereas the equatorial streak can be attributed to the formation of a bundle of chains or microfibrillar structures parallel to the flow direction [32]. The observation of the equatorial streak can also be explained as the formation of $a$*-axis-oriented 'daughter' lamellae growing epitaxially. The SAXS pattern seen indicates the existence of shish-kebab-like morphology at the depth of 100 μm in iPP-3, and for comparison Fig. 3 shows the SAXS image patterns obtained from the depth of 100 μm of iPP-1 and iPP-5. They are similar to the oriented image pattern as

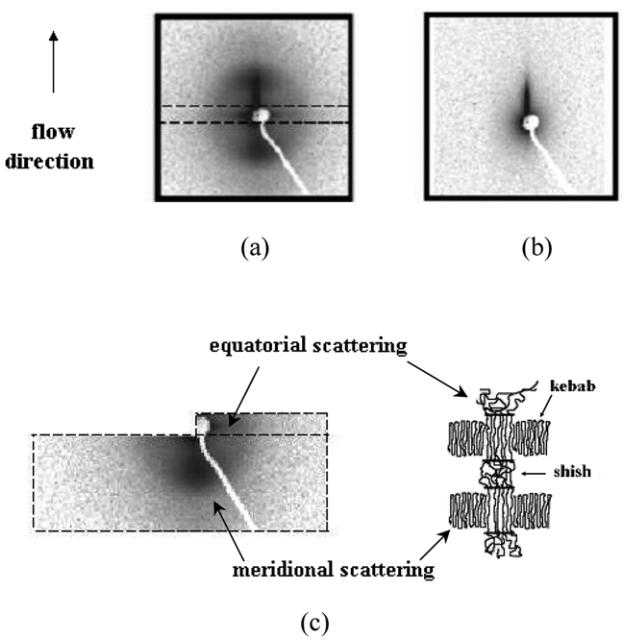


Fig. 2. (a) A two-dimensional SAXS image pattern at 100 μm from the surface of an iPP-3 plate in the depth direction. (b) 2D SAXS pattern of air as scattering background. (c) Sections of (a) for calculation of integrated SAXS intensities along the equatorial and meridional directions.

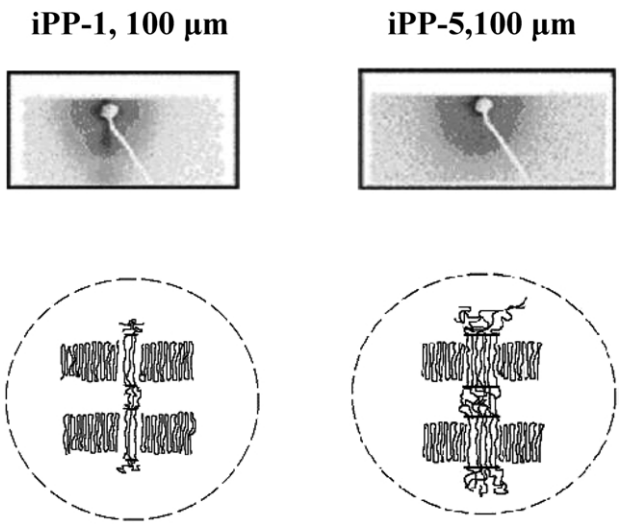


Fig. 3. Two-dimensional SAXS image patterns at 100 μm from the surface of iPP-1 and iPP-5 plates.

shown in Fig. 2, with two reflections along and normal to the flow direction observed. It is found, however, that the magnitude of the scattering maxima is strongly dependent on the thickness of the plates, although all samples were injection-moulded under the same conditions. Compared with the case of iPP-3, a stronger and narrower meridional maximum is seen from the iPP-1 pattern whereas a very weak and broad meridional maximum is detected from the iPP-5. On the other hand, the magnitude of the equatorial streak of iPP-5 is visibly significant but the equatorial streak of iPP-1 is more smeared.

It is generally accepted that melt-shear causes the development of oriented primary row nuclei that subsequently generate an epitaxial growth of folded chain lamellae perpendicular to the row nuclei [4,18,29]. Our observations confirm the formation of shear-induced row nuclei in the form of microfibrillar bundles at a depth of 100 μm from the surface, regardless of the thickness of the plates. Since the level of effective melt-shear imposed on the polymer melt rapidly attenuates with increasing thickness of the plate, the epitaxial growth of oriented polymer lamellae from the row nuclei formed during the primary nucleation should be strongly dependent on the thickness. The results indicate that at 100 μm folded chain lamellae in the iPP-1 melt start to grow rapidly from the row nuclei along the epitaxial direction even if the concentration of row nuclei is still low, which leads to the formation of shish-kebab morphology. The effective melt-shear, however, seems not to be high enough to promote immediately an epitaxial growth of the iPP-5 melt. On the basis of the SAXS patterns, the resultant morphologies are schematically shown in Fig. 3.

The morphological development toward the core region is presented in Fig. 4. The SAXS image pattern at 200 μm of iPP-1 is similar to that observed at the depth of 100 μm, as shown in Fig. 3, and the morphology of iPP-1 remains a

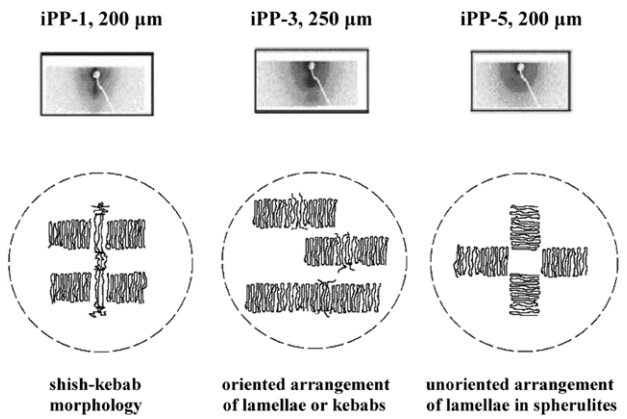


Fig. 4. Two-dimensional SAXS image patterns at 200 μm from the surface of iPP-1 and iPP-5 plates and at 250 μm from the surface of an iPP-3 plate.

shish-kebab-like structure. However, the equatorial streak of iPP-3 is not detectable from the SAXS image pattern at the depth of 250 μm, although the meridional maximum figure shows, qualitatively, not much change. Obviously, the absence of an equatorial streak indicates that the morphology of iPP-3 at 250 μm is no longer a typical shish-kebab-like structure, but stacks of oriented crystalline lamellae or kebabs only. The SAXS image pattern at 200 μm of iPP-5 looks like the morphology that is observed in quiescent crystallization, although, in comparison with the morphology of the core region; the possible existence of orientation at 200 μm may not be totally ruled out. At the core region, the SAXS image patterns of all samples show isotropic features, as shown in Fig. 5.

It is worth noting that the missing equatorial streak at 250 μm of iPP-3 cannot be considered as the absence of the shish structure. According to the mechanism of shear-induced crystallization of polymer melts [4,18,29], if the linear row nuclei or shishes did not form, the nucleation and growth of kebabs or lamellae perpendicular to the flow direction would not be possible. The observation of kebab-like structure in the 2D SAXS image pattern indicates that the shear-induced shish-like structure should exist. The size of isolated shish structures is so small or the concentration

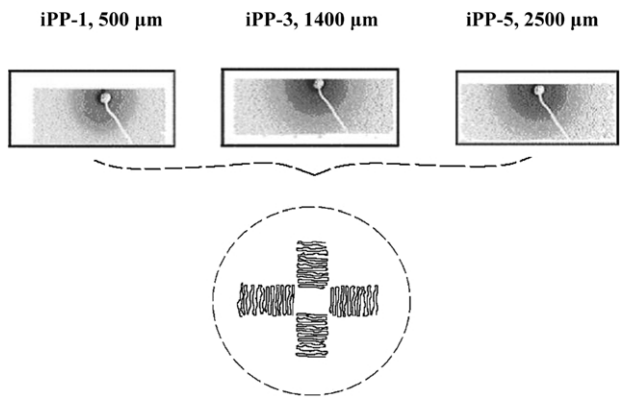


Fig. 5. Two-dimensional SAXS image patterns at the core region of iPP-1, iPP-3, and iPP-5 plates.

of shishes is so low that SAXS cannot easily detect the structure in the present work due to the limits of resolution. The other explanation of the missing equatorial streak may be that the kebab structure observed at 250 μm of iPP-3 is actually the part of the whole shish-kebab structure that is developed from the surface during the shear-induced crystallization. The shish-like structure may exist closer to the surface and spatially far away from the illuminated zone of X-ray beam.

The above findings indicate that under the same injection ram speed and the same melt and mould temperatures, the different levels of effective shear flow are internally imposed on the polymer melt. For example, the maximum shear strain rate at wall decreases with increasing the thickness of the plate. Depending on the thickness of the plate, the gradient of melt-shear from the surface to the core may or may not effectively modify the kinetics of crystallization and the morphological distribution. Under the present injection moulding conditions, the iPP-5 melt starts to undergo crystallization almost in the absence of a shear field at depths that are very close to the surface. The morphological feature of the iPP-5 at 200 μm and hereafter is expected to be the stacks of random crystalline lamellae due to a low level of shear flow. On the other hand, the effective shear at the same region of iPP-1 and iPP-3 is sufficient high to induce, respectively, the shish-kebab-like morphology and oriented crystalline lamellae.

The integrated intensities of SAXS, $I_{\text{meridian}}$ and $I_{\text{equator}}$, were calculated by sectioning the SAXS images patterns in a way as shown in Fig. 2(c) in order to obtain quantitatively the morphological distribution along the thickness of injection-moulded plates. The narrow meridional and equatorial areas were extracted in order to eliminate the reflection of integrated intensity from entire 2D SAXS image patterns. The background scattering was subtracted from the raw data. The values of integrated intensities were calculated only from one side of the specimen and a symmetric distribution was assumed.

The distributions of integrated intensities, $I_{\text{meridian}}$ and $I_{\text{equator}}$, through the thickness of the plate are presented in Fig. 6. The magnitude of $I_{\text{equator}}$ does not vary greatly with the depth, although its distribution shows a somewhat down-U curvature, increasing toward the centre of the moulding. On the other hand, $I_{\text{meridian}}$ decreases toward the centre of the plate in the core region. Unlike $I_{\text{equator}}$, the magnitude of $I_{\text{meridian}}$ is found to depend on the thickness of the plate. It can be seen from Fig. 6 that the values of $I_{\text{meridian}}$ of iPP-5 at the surface region are much smaller than those of thin plates, although the shape of the distribution is similar. A highest value of $I_{\text{meridian}}$ observed at 250 μm in the distribution of iPP-3 would indicate the position sensitivity of $I_{\text{meridian}}$. The results show that under the present injection moulding conditions, the increase of the shear through the reduction of thickness can only affect the epitaxial growth of lamellae or the lamellar orientation along the flow direction. However, once the thickness of plate in an industrial process is lower than a certain value (or the effective shear imposed on the polymer melt exceeds a certain value), further reduction in the thickness would not cause a significant change in the morphological distribution. This can be evidenced qualitatively from the distributions of iPP-1 and iPP-3 in Fig. 6. The quantitative results will be given from the calculations of lamellar orientation and lamellar thickness.

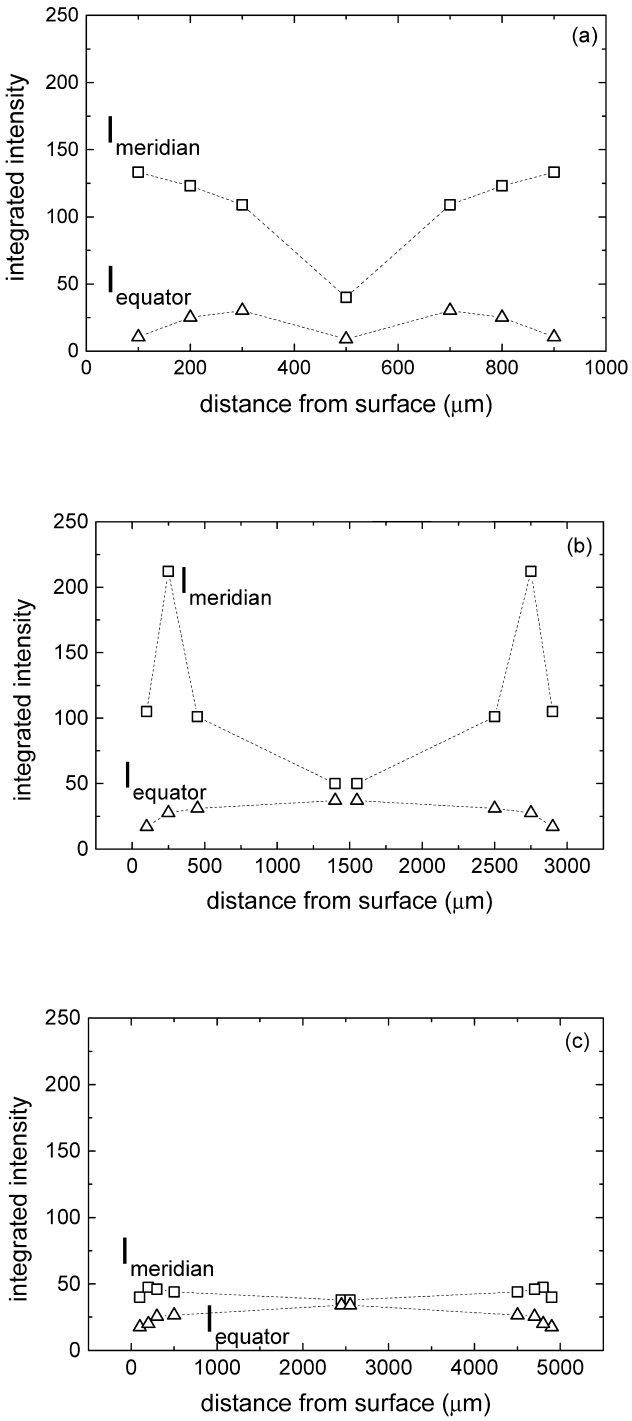


Fig. 6. Distributions of integrated SAXS intensities of equatorial and meridional scattering in the depth direction of injection-moulded plates: (a) iPP-1, (b) iPP-3, and (c) iPP-5. Insert is enlargement of (c).

Note that the integrated intensities of each SAXS pattern are the contribution of all scatterers in the polymer. For injection-moulded polymers, the segments of polymer chains align along the flow direction upon the imposition of melt-shear and the orientation-induced nuclei would be produced from the primary nucleation. These nuclei provide nucleating sites for the growth of crystallites through the second nucleation after cessation of shear. It should be pointed out, however, that in the above discussion we emphasize the thickness dependence of shish-kebab-like structures at the surface region. The existence of such a structure does not mean that there are only oriented crystallites at the surface region even at 100 μm. Because the growth rate of crystallization is independent of the type of nucleation, the lamellae can grow from points, surfaces, or be row nucleated [33]. It is not doubt that both oriented crystallites and randomly distributed crystallites exist in the surface region of final polymer plates. Accordingly, the integrated intensities of SAXS have oriented and unoriented components. The oriented scattering is from oriented lamellae while the unoriented component includes the scattering from randomly distributed crystalline lamellae and the Compton scattering from chemical structures. The Compton scattering is negligibly small.

In order to describe the level of lamellar orientation along the flow direction and subsequently to obtain the distribution of preferentially oriented crystalline lamellae through the thickness of the plate, the integrated meridional intensity in the core region, $I_{\text{meridian}}(\text{core})$, which is attributed to the isotropic scatters, was subtracted from the integrated intensity $I_{\text{meridian}}$ at each depth. The values of $I_{\text{meridian}} - I_{\text{meridian}}(\text{core})$ at each depth were then normalized by division of $I_{\text{equator}}$ at the corresponding depth to define a preferential orientation index, $\eta_{\text{I}}$, as follows:

$$\eta_{\text{I}} = \frac{I_{\text{meridian}} - I_{\text{meridian}}(\text{core})}{I_{\text{equator}}} \tag{2}$$

This index gives a relative measure, as a first approximation, of the orientation of crystalline lamellae along the flow or meridional direction. The distributions of $\eta_{\text{I}}$ calculated from three samples are illustrated in Fig. 7. As can be seen, the influence of thickness of plates on the preferential orientation of crystalline lamellae is much stronger for the thin plate than for the thick one. In comparison with the isotropic core, the thin plate has experienced much stronger melt-shear during the injection moulding process. The effective melt-shear field imposed on the polymer melt is dramatically reduced once the thickness of plate is increased to a certain value.

The structural parameters of lamellae, including the thickness of the crystalline lamellae $L_{\text{c}}$, the thickness of the amorphous lamellae $L_{\text{a}}$, the long spacing $L$, and the degree of linear crystallinity $x_{\text{l}}$, were investigated in order to provide further details of the effects of plate thickness on the formation of morphological distribution. The

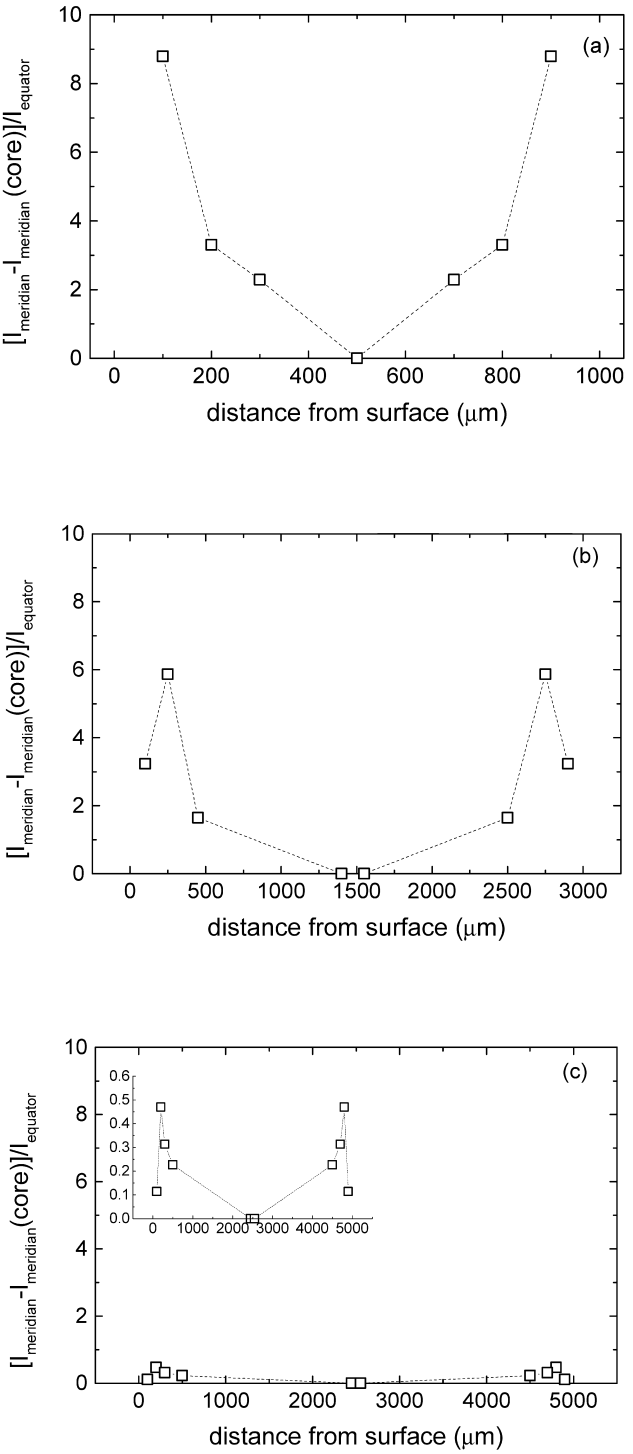


Fig. 7. Distributions of preferential orientation index along flow direction, $\eta_{\text{I}}$, in the depth direction of injection-moulded plates: (a) iPP-1, (b) iPP-3, and (c) iPP-5.

one-dimensional correlation function of the Fourier transform of SAXS profiles in real space was used in the present work [33,34]. In the one-dimensional correlation function analysis, it is assumed that the lamellar stacks are perfectly oriented and are infinitely high. The scattering from such an ideal stack should be a pair of discrete peaks along the

stacking direction. However, since the lamellar stacks in a real system cannot be perfectly parallel to each other, the scattering in reciprocal space is actually spread over an area of the reflecting sphere, this area being proportional to $q^2$. The Lorentz correction is used to correct a system so as to be a perfect orientation in the one-dimension correlation function analysis [34]. Ruland has shown [36] that the one-dimension correlation function can be applied for meridional intensity distribution of any partially oriented system in the same way as for an isotropic system, except for a completely orientated case like fibers. Fig. 8 shows typical Lorentz-corrected meridional intensity profiles of three samples at the selected depths.

The normalized one-dimensional correlation function is defined as [34,35]

$$\nu(z) = \frac{\int_0^\infty [I(q) - I_t - I_b(q)]q^2\cos(qz)\mathrm{d}q}{Q_I} x \quad (3)$$

where $Q_I = \nu(0)$ is a scattering invariant and $I_t$ is the background intensity arising from thermal density fluctuations. The invariant $Q_I$ is independent of the size and shape of scattering entities and is a quadratic function of both the volume fraction of crystals $\phi$ and the electron density difference, $\Delta\eta$, between the two phases. For a two-phase system with a sharp boundary, the invariant $Q_I$ is given by

$$Q_I = \int_0^\infty [I(q) - I_t(q) - I_b(q)]q^2\mathrm{d}q = A\phi(1-\phi)\Delta\eta^2 \quad (4)$$

where $A$ is a constant related to experimental conditions. The two-phase model has been extended to a pseudo-two-phase model to include a transition layer or interface of smooth electron density between the crystalline and amorphous lamellae [37]. The structural parameters of lamellae can be graphically obtained from the correlation function. In the present work, the interface distribution function $g_1(z)$ was used to determine the structural parameters. The interface distribution function $g_1(z)$ is given by the second derivative of the one-dimensional correlation function $\nu(z)$ [38].

$$g_1(z) = \nu''(z) \quad (5)$$

The subtraction of $I_t$ from the measured intensity $I$ is essential for the application of the one-dimensional correlation function. The magnitude of $I_t$ can be estimated for the present work by the application of the slit-smeared form of modified Porod's law: [39]

$$\lim_{q\to\infty} I(q) = \frac{K_p'}{q^3} + I_t \quad (6)$$

where $K_p'$ is a constant related to the Porod constant $K_p$ [22]. $I_t$ can be obtained from a regression analysis of Eq. (6) in the range of higher $q$ (Porod range). In the present work, the scattered intensity arising from thermal density fluctuations is very small.

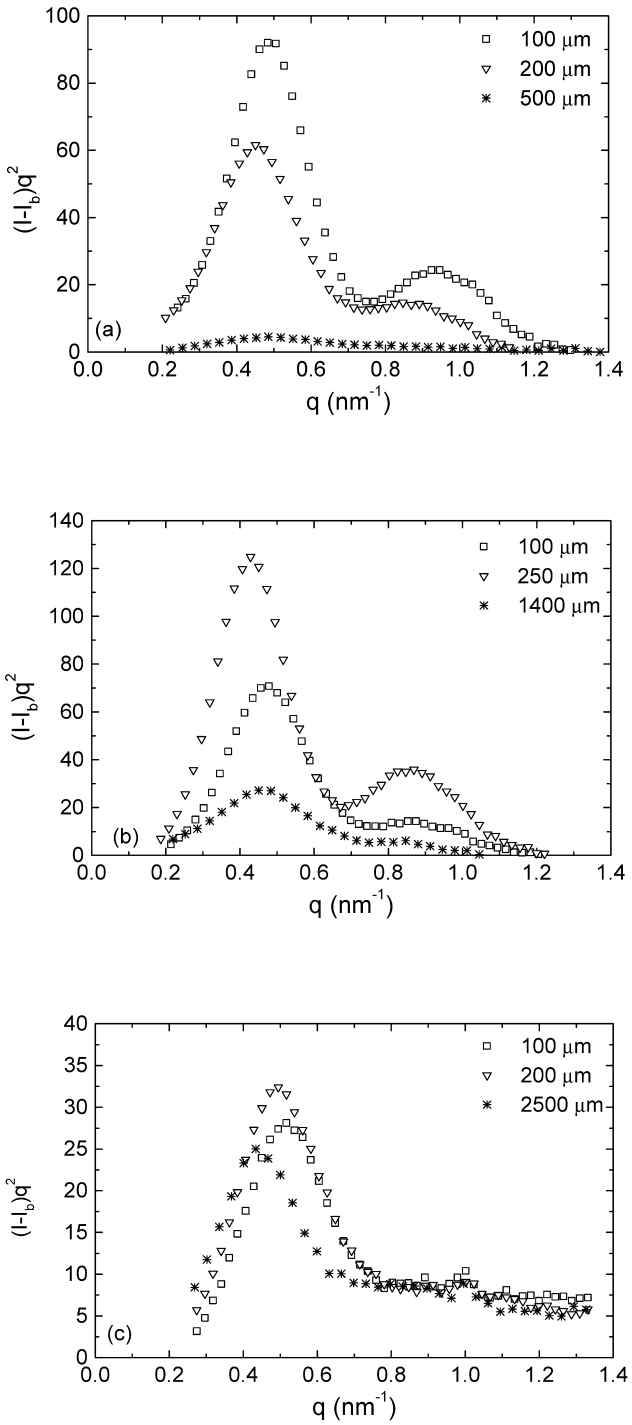


Fig. 8. Lorentz-corrected SAXS intensity profiles along the meridian at selected depths of injection-moulded plates: (a) iPP-1, (b) iPP-3, and (c) iPP-5.

Fig. 9 shows typical plots of the interface distribution function $g_1$ for three samples at the surface region and at the core. Since the lamellar dimensions are not a constant throughout the whole sample but have distributions [40], the values obtained are average ones. The average value of the long spacing $\langle L\rangle$, which represents the most probable distance between two adjacent crystalline lamellae, can be

obtained from the first minimum of $g_1$. The first maximum of the interface distribution function, however, gives the average thickness of either crystalline lamellae $\langle L_c \rangle$ or that of amorphous lamellae $\langle L_a \rangle$. Assignments of lamellar thickness, however, cannot be done from the interface distribution function alone on the basis of Babinet's reciprocity theorem [41], because the thickness of the crystalline lamellae $\langle L_c \rangle$ cannot be distinguished from the thickness of amorphous lamellae $\langle L_a \rangle$. Therefore, the smaller length and the larger length obtained are first denoted by $\langle L_1 \rangle$ and $\langle L_2 \rangle (= \langle L \rangle - \langle L_1 \rangle)$, respectively. Such results obtained are shown in Fig. 10. It is found that the values of long spacing of iPP-1 and iPP-3 are higher than that of iPP-5. The distinguishable difference in the long spacing between iPP-1 and iPP-3 is that the variation of $\langle L \rangle$

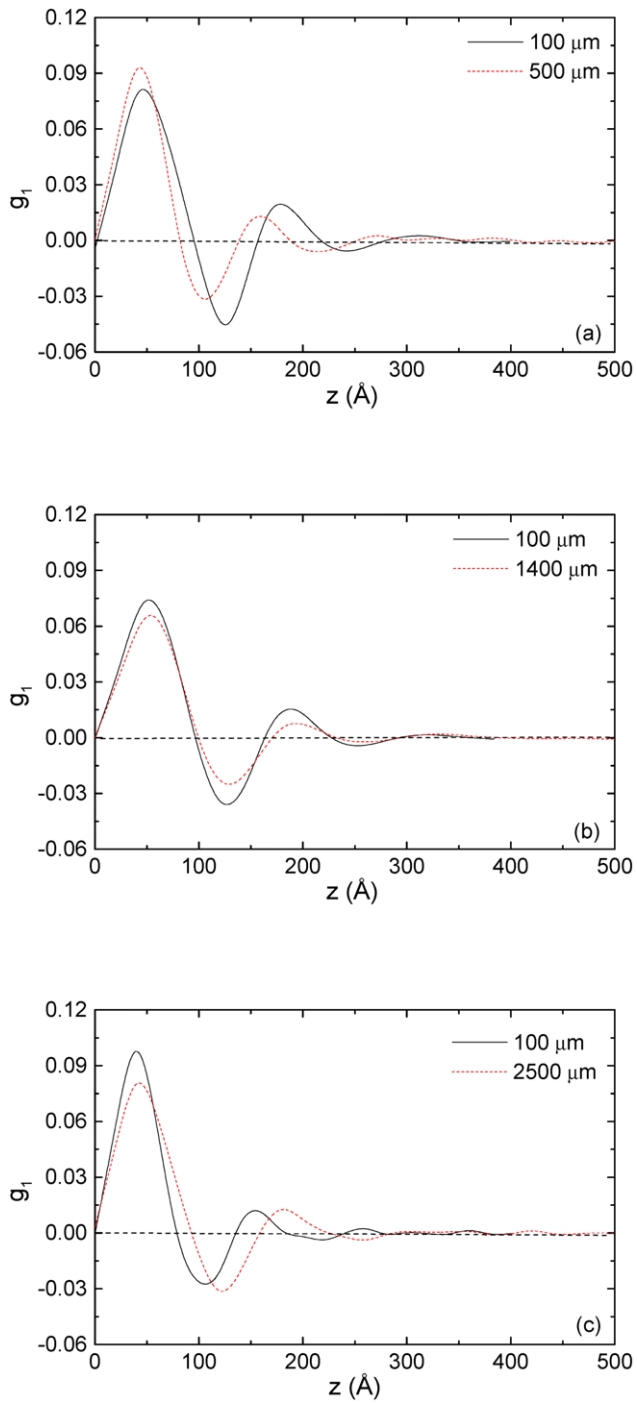


Fig. 9. One-dimensional interface distribution functions, $g_1(z)$, along the meridian at selected depths of injection-moulded plates: (a) iPP-1, (b) iPP-3, and (c) iPP-5.

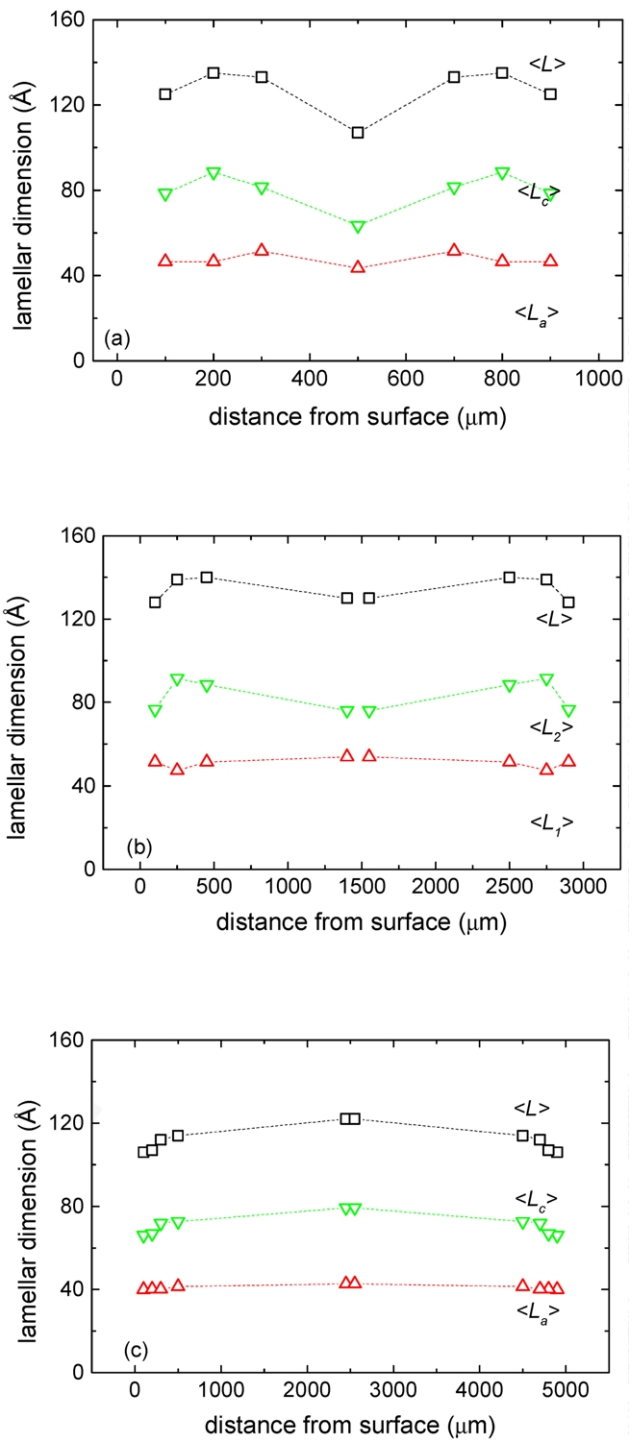


Fig. 10. Distributions of lamellar dimensions along the meridian in the depth direction of injection-moulded plates: (a) iPP-1, (b) iPP-3, and (c) iPP-5.

with the depth is more significant in iPP-1 than that in iPP-3. As the thickness of plate is increased to 5 mm, the distribution of $\langle L \rangle$ tends to be a weak down U-shape, which is normally found in the quiescent crystallization of polymers.

It is known that the degree of linear crystallinity $x_l$ is related to the degree of volume crystallinity $x_v$ by Refs. [38,42–44]

$$x_v = \varphi x_l \tag{7}$$

where $\varphi$ is the volume fraction of the lamellar stacks in a sample. The value of the fraction $\varphi$ is equal to unity if the whole volume of a sample is perfectly filled with lamellar stacks. Since the volume fraction outside the lamellar stacks is always filled with amorphous material [42–44], especially when polymers have low degrees of volume crystallinity, the degree of volume crystallinity $x_v$ is never higher than that of linear crystallinity $x_l$. The degrees of volume crystallinity of all three samples have been calculated using wide-angle X-ray data in the conventional way [30,45]. The values of volume crystallinity, for example, iPP-3, are 0.4–0.43. If the degree of linear crystallinity of iPP-3 is assumed to be smaller than 0.5, the values of $\langle L_1 \rangle$ obtained from iPP-3 should be assigned as those of thickness of crystalline lamellae and corresponding values of linear crystallinity are 0.34–0.42. Obviously, the assumption of $x_l < 0.5$ is physically not valid because $x_l < x_v$ suggests that more than 100% space is filled with lamellar stacks. The same conclusion was also obtained for almost all of data of iPP-1 and iPP-5. Even for the few cases where $x_l$ is marginally larger than $x_v$ in the core, the assumption $x_l < 0.5$ for the present work leads an unrealistic jump in the linear crystallinity. On the basis of the above analysis, the larger length $\langle L_2 \rangle$ and the smaller length $\langle L_1 \rangle$ are appropriately denoted as $\langle L_c \rangle$ and $\langle L_a \rangle$, respectively. The degree of linear crystallinity is thus always larger than 0.5 in the present work.

The degree of linear crystallinity $x_l$, which represents the fraction of crystalline lamellae in individual stacks, is calculated accordingly by

$$x_l = \frac{\langle L_c \rangle}{\langle L_c \rangle + \langle L_a \rangle} = \frac{\langle L_c \rangle}{\langle L \rangle} \tag{8}$$

Fig. 11 shows the distribution of the linear crystallinity $x_l$. Generally, the change in the thickness of the moulding leads to change in the distribution of linear crystallinity under the particular injection moulding conditions, that is, the degree of linear crystallinity is dependent not only on the distance from the surface but also on the thickness of the plate. The imposition of shear flow on polymer melts or the crystalline precursors enhances the crystallization of the polymer melt and the ordered packing of lamellar stacks. The shape of the crystalline distribution is quite different at the selected positions of three samples. As can be seen, the degree of linear crystallinity of iPP-1 and iPP-3 proceeds through two sequential stages on moving from the surface region to the core: the degree of $x_l$ first increases to a maximum and then declines toward to the core region. On the other hand, the degree of linear crystallinity of iPP-5 is almost independent of position through the plate. The distribution of linear crystallinity $x_l$ obtained from iPP-3 is similar to that of the preferential orientation index of crystalline lamellae,

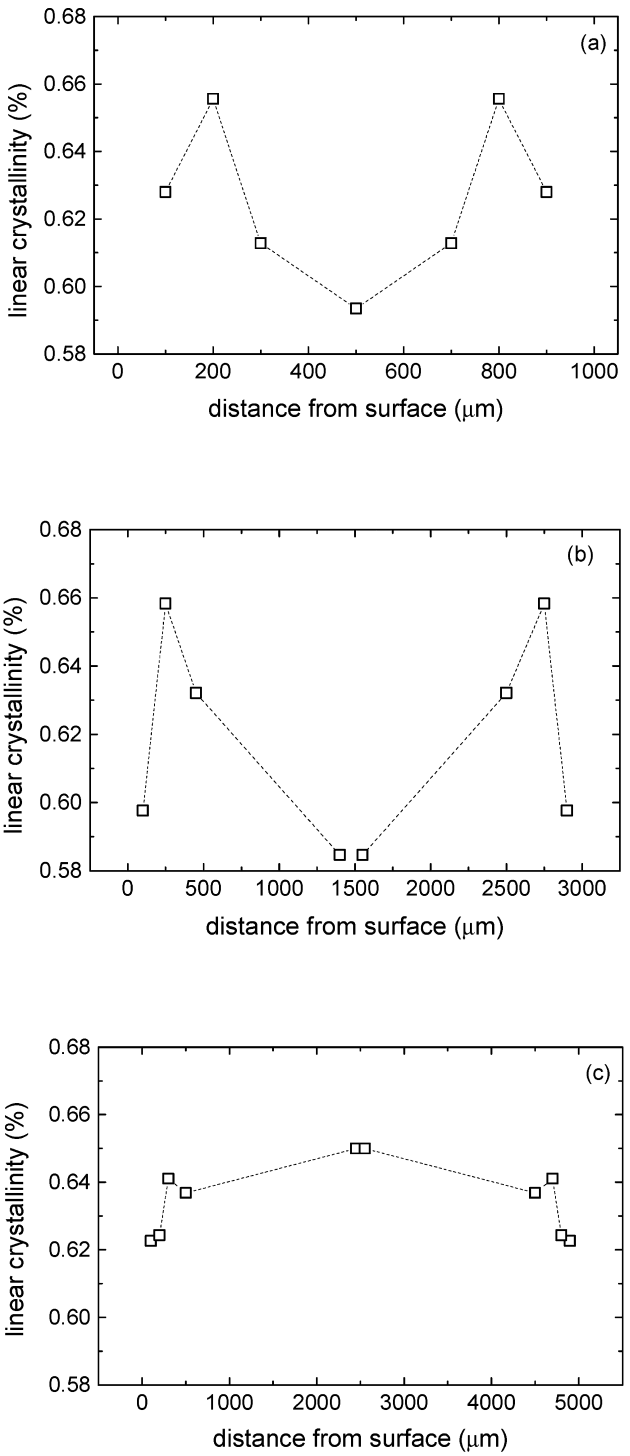


Fig. 11. Distributions of degree of linear crystallinity along the meridian in the depth direction of injection-moulded plates: (a) iPP-1, (b) iPP-3, and (c) iPP-5.

implying that higher degrees of linear crystallinity correspond to higher levels of lamellar orientation. Note that this consistence is not always observed. The highest degree of linear crystallinity appears at 200 μm from the surface of iPP-1 whereas the highest level of preferential orientation index $\eta_l$ is observed at 100 μm, although both depths are not beyond the surface region.

Compared with the distribution of linear crystallinity of thin plates, the degree of linear crystallinity of iPP-5 tends to increase in the core region. Such a phenomenon suggests that, in addition to the melt-shear flow, the degree of linear crystallinity is also affected by the cooling rate of polymer melts during solidification. In the core region, the slower cooling rate of the thick plate allows more complete relaxation of polymer chains during crystallization, which results in a higher degree of linear crystallinity.

## 4. Conclusions

The effects of thickness of injection-moulded iPP plates on the shear-induced morphological distribution were investigated using synchrotron small-angle X-ray scattering. The iPP specimens were cut from the centre of each plate, and the experiments were designed in such a way that the square X-ray beam vertically passed through the section and the illuminated zone was changed with a vertical shift of the sample holder along the direction of the plate thickness. The microstructures and their distributions were evaluated using SAXS. The morphological development through the plates was then obtained from the discrete reflections of a series of two-dimensional SAXS image patterns.

Shish-kebab-like morphology is detected around 100 μm from the surface of the plates due to the shear flow. The formation of shish-kebab-like morphology in the surface region is consistent with the mechanism of the row nuclei being induced in the form of microfibrillar bundles on which the folded chain lamellae grow epitaxially from the surface region to the core. However, a careful examination shows that as the thickness of the moulding is increased to 5 mm the intensity of discrete reflections in the image pattern is very weak at 100 μm and the shish is found to be dominant structure in the shish-kebab morphology. It can be anticipated that with a further increase in the thickness of plate, the kebab structure would not be detectable under the current injection moulding conditions, although the formation of a few uncorrelated kebabs is not impossible.

A dramatic change in the shear-induced morphology is observed as the depth from the surface of the plate is increased to 200 μm. Although this depth is generally not beyond the surface region, an isotropic scattering emerges from the SAXS image pattern of iPP-5. The shish-kebab morphology remains at 200 μm in iPP-1 whereas the equatorial streak disappears from the SAXS image pattern at 250 μm in iPP-3. The findings indicate that in the early stage of crystallization, the effective melt-shear is sufficiently high to maintain a certain level of a preferentially oriented growth of row nucleated in the iPP-1 melt at the depth of 200 μm but is too low to do so for the iPP-5 melt at the same depth. The different types of nucleation in the iPP-5 melt, including point and surface nucleated, have almost the same growth rate of crystallization at 200 μm under external melt-shear, which results in the formation of randomly oriented crystallites.

Although the melt-shear causes a slight difference in the linear crystallinity, the preferential orientation of crystalline lamellae along the flow direction exhibits strong thickness dependence. The preferential orientation index of iPP-1 in the surface region is about nine times larger than that near the core while the index of iPP-5 is negligibly small even near the surface region. It can be concluded that if the external melt-shear is not sufficient (or equivalently, the plate is too thick), the growth of crystalline lamellae can occur in a way similar to quiescent crystallization, once the shear-induced row nuclei form. In addition to melt-shear, it is also found that the cooling rate of polymer melts also affect the linear crystallinity. In the core region, a slow relaxation of polymer chains in the thick plate can lead to a higher degree of linear crystallinity.

## Acknowledgements

This work was performed at the Australian National Beamline Facility (ANBF) with support from the Australian Synchrotron Research Program, which is funded by the Commonwealth of Australia under the Major National Research Facilities Program.

## References

[1] Meijer HEH, editor. Processing of polymers, vol. 18.; 1997. VCH. Weinheim, Germany.
[2] Keller A, Kolnaar HWH. Flow induced orientation and structure formation. In: Meijer HEH, editor. Processing of polymers, vol. 18. Weinheim, Germany: VCH; 1997.
[3] Lee O, Kamal MR. Polym Engng Sci 1999;39:236.
[4] Kumaraswamy G, Issaian GA, Kornfield JA. Macromolecules 1999; 32:7537.
[5] Rueda DR, Ania F, Balta-Calleja FJ. Polymer 1997;38:2027.
[6] Eder G, Janeschitz-Kriegl H. Colloid Polym Sci 1988;266:1087.
[7] Gao X, Isayev AI, Guo L. Polym Engng Sci 1999;39:2096.
[8] Coppola S, Grizzuti N, Maffettone PL. Macromolecules 2001;34: 5030.
[9] Trotignon JP, Lebrun JL, Verdu J. Plast Rubber Process Appl 1982;2: 247.
[10] Zipper P, Janosi A, Geymayer W, Ingolic E, Fleischmann E. Polym Engng Sci 1996;36:467.
[11] Kantz MR, Newman HD, Stigale JFH. J Appl Polym Sci 1972;16: 1249.
[12] Mencik Z, Fitchmun DR. J Polym Sci, Polym Phys Ed 1973;11:973.
[13] Fujiyama M, Kimura S. J Appl Polym Sci 1978;22:1225.
[14] Kalay G, Bevis MJ. J Polym Sci, Polym Phys Ed 1997;35:265.
[15] Katti SS, Schultz JM. Polym Engng Sci 1982;22:1001.

[16] Kumaraswamy G, Kornfield JA, Fengji Y, Hsiao BS. Macromolecules 2002;35:1762.
[17] Keller A, Kolnaar HWH. Mater Sci Technol 1997;18:189.
[18] Eder G, Janeschitz-Kriegl H, Liedauer S. Prog Polym Sci 1990;15: 629.
[19] Ania F, Bayer RK, Tschmel A, Michler HG, Naumann I, Balta-Calleja FJ. J Mater Sci 1996;31:4199.
[20] Jerschow P, Janeschitz-Kriegl H. Int Polym Process 1997;12:72.
[21] Andersen PG, Carr SH. J Mater Sci 1975;10:870.
[22] Clark ES, Spruiell JE. Polym Engng Sci 1976;16:176.
[23] Lovinger AJ. J Polym Sci, Polym Phys Ed 1983;21:97.
[24] Fujiyama M, Wakino T, Kawasaki Y. J Appl Polym Sci 1988;35:29.
[25] Khoury F. J Res Natl Bur Stand 1966;A70:29.
[26] Lotz B, Wittmannn JC. J Polym Sci, Polym Phys Ed 1986;24:1541.
[27] Wilkinson AN, Ryan AJ. Polymer processing and structure development. Dodrecht: Kluwer; 1998.
[28] Varga J. J Mater Sci 1992;27:2557.
[29] Somani RH, Hsiao BS, Nogales A, Srinivas S, Tsou AH, Sics I, Balta-Calleja FJ, Ezquerra TA. Macromolecules 2000;33:9385.
[30] Zhu PW, Edward G. Macromol Mater Engng 2003;288:301.
[31] Baird DG, Collias DI. Polymer processing. USA: Butterworth-Heinemann; 1995.
[32] Schultz JM, Hsiao BS, Samon JM. Polymer 2000;41:8887.
[33] White HM, Bassett DC. Polymer 1997;38:5515.
[34] Strobl GR. The physics of polymers. New York: Springer; 1997.
[35] Vonk CG, Kortleve G. Koll Z.-Z. Polym 1967;220:19.
[36] Ruland W. J Appl Crystallogr 1971;4:70.
[37] Ruland W. Colloid Polym Sci 1978;256:932.
[38] Cruz CS, Stribeck N, Zachmann HG, Balta-Calleja FJ. Macromolecules 1991;24:5980.
[39] Koberstein J, Stein JR. J Polym Sci, Polym Phys Ed 1983;21:2181.
[40] Ruland W. Acta Crystallogr 1961;4:1180.
[41] Cowley JM. Diffraction physics. Amsterdam: North-Holland; 1981.
[42] Chen HL, Li LJ, Lin TL. Macromolecules 1998;31:2255.
[43] Verma RK, Marand H, Hsiao BS. Macromolecules 1996;29:7767.
[44] Medellin-Rodriguez FJ, Phillips PJ, Lin JS, Campus R. J Polym Sci; Polym Phys 1997;35:1757.
[45] Zhu PW, Edward G. Manuscript in preparation.